Science Advances
AAAS

advances.sciencemag.org/cgi/content/full/6/32/eaba7573/DC1

Supplementary Materials for

Highly variable upper and abyssal overturning cells in the South Atlantic

M. Kersalé*, C. S. Meinen, R. C. Perez, M. Le Hénaff, D. Valla, T. Lamont, O. T. Sato, S. Dong, T. Terre, M. van Caspel, M. P. Chidichimo, M. van den Berg, S. Speich, A. R. Piola, E. J. D. Campos, I. Ansorge, D. L. Volkov, R. Lumpkin, S. L. Garzoli

*Corresponding author. Email: marion.kersale@noaa.gov

Published 5 August 2020, *Sci. Adv.* **6**, eaba7573 (2020)
DOI: 10.1126/sciadv.aba7573

This PDF file includes:

Data and Methods

In this study, moorings in the South Atlantic MOC Basin-wide Array (SAMBA) at 34.5°S are used to estimate the absolute meridional geostrophic transports associated with the western and eastern boundary currents as well as the interior flows. The array consists primarily of Pressure-equipped Inverted Echo Sounder (PIES) moorings, some of which are also equipped with a near-bottom current meter (CPIES). In its present configuration, there are approximately 20 SAMBA moorings of different types active at any given time. However, the focus here is on the nine PIES and CPIES instruments on the western and eastern boundary that have provided continuous daily observations from September 2013 to July 2017 (see Table S1 and Fig. 1 for locations). Since we do not use the near-bottom current meter data from the CPIES in this study, hereafter we simply refer to the CPIES as PIES. The modern techniques involved in analyzing PIES data to estimate volume transports have been widely discussed, and only a brief description of the methodology is provided here. For additional details of how this methodology has been adapted to 34.5°S see papers by *(21, 22, 39)*.

A PIES measures both the bottom pressure and the round-trip time for an acoustic signal to travel vertically from the bottom-moored instrument to the sea surface and back. All hourly PIES travel time (τ) and bottom pressure records were low pass filtered using a second order Butterworth filter passed both forward and backward to avoid phase shifting – the cutoff period for the filter was 72 hours. Tidal response analysis *(40)* determined semidiurnal and diurnal tidal bottom pressure constituents for each instrument; these tidal constituents were subtracted from the bottom pressure time series prior to filtering. The final filtered hourly τ and bottom pressure measurements were then subsampled to one value per day at noon UTC.

The Gravest Empirical Mode (GEM) technique allows the τ record from a PIES to be combined with historical hydrographic data from the region to produce estimated full-water-column profiles of temperature, salinity, density, and/or dynamic heights *(34)*. Previously, these analyses have been successfully generated on the western boundary *(8)*, eastern boundary *(39)*, or on both boundaries *(21, 22)*. A data set of 378 CTD and 5215 Argo profiles on the eastern boundary, and of 485 CTD and 3332 Argo profiles on the western boundary, are available from 1983 up to the present day (Fig. S1, upper panels). These profiles are used to create the GEM lookup tables along each boundary (Fig. S1, middle panels). Zonal gradients in density or dynamic height profiles between neighboring PIES yield full-water-column profiles of the baroclinic (density-driven) component of the geostrophic velocity relative to an assumed level of no motion (i.e., the reference level). Only the component of horizontal velocity which is orthogonal to the transect between PIES is provided (i.e., meridional velocity across our zonal transect). With the GEM method, we use the scatter between the original data (CTD and Argo) and the resulting smoothed lookup tables to provide a natural “accuracy estimate” for the GEM fields (Fig. S1, lower panels). This scatter represents the true ocean variability about the GEM temperature and salinity fields. The root-mean-square differences between the smoothed GEM field and the original CTD and Argo data in the example presented for the western and the eastern boundaries range from about 1.5°C for temperature at the surface (where seasonal variability is maximum) down to around 0.05-0.3°C in the deep ocean. Adding more hydrographic casts in the future will yield better coverage of the τ parameter space, but essentially the same accuracy for the GEM field *(39)*.

The absolute geostrophic velocity at the reference level is estimated from the zonal gradients in bottom pressure between each pair of PIES *(34)*. Differences in bottom-pressure measured between the

PIES provide the temporal-variations of the barotropic (pressure-driven) component of the absolute geostrophic velocity. Due to the well-known 'leveling' problem *(40)*, the bottom pressure differences can provide only the time variability of the reference velocity. For this study the time-mean velocity at 1500 dbar from the Estimating the Circulation and Climate of the Ocean, Phase 2 (ECCO2; https://ecco.jpl.nasa.gov/) ocean state estimate was added to the time-varying bottom-pressure derived reference velocity variability to produce the absolute reference level velocities. This time-varying reference velocity was added to the PIES-GEM relative velocity profiles to yield full-water column time series of absolute velocity perpendicular to the transect between moorings. The ECCO2 output was also used to provide a time-invariant estimate of the flows on the continental shelves/upper slopes inshore of the shallowest moorings following previous methods *(21, 22)*. Using a different numerical model, like the free-running Ocean general circulation model For the Earth Simulator (OFES, see *(21)* for more details about the use of this model for referencing MOC volume transport), instead of ECCO2 did not substantially alter the mean transport results (not shown). We chose ECCO2 because its ocean state is constrained by observations (N.B., no SAMBA data are used in constraining the model). Finally, the Ekman transports were estimated using the winds from the cross-calibrated multiplatform (CCMP) product version 2.0 *(37)* as in *(21)*.

The resulting total basin-wide meridional absolute velocity is determined as the sum of the above components; this total was then zonally integrated to produce full-depth profiles of transport per unit depth from the surface down to ~4700 dbar. The deep transport calculations and integrations (below ~1500 dbar) must take into account the highly variable topography in the abyssal ocean (eastern and western slopes, and Mid-Atlantic-Ridge). Integrating geostrophic velocities in the presence of this topographic complexity leads to regions known as 'bottom triangles' that are not sampled. To estimate the transports within these areas, the PIES-GEM density profiles are first vertically extrapolated below their deepest common depth using the GEM lookup tables. The transport within these areas are then estimated geostrophically, taking into account the ratio between the ocean area and the portion of the span between mooring sites that is below the sea-floor. The impact of the bottom triangles on the abyssal transport accuracy estimate is presented in the following section.

To produce volume transport estimates of the upper and abyssal MOC cells, the transport per unit depth profiles were integrated vertically. The vertical integration limits were determined based on the changes in sign of either the record-length time-mean transport per unit depth profile or of the record-length time-mean cumulative vertical integral of the transport per unit depth. For the upper MOC cell, the vertical integration limits were from the sea surface down to the point where the time-mean zonally-integrated flow (i.e., the transport per unit depth profile) changes from northward to southward (at 1315 dbar; red dot in Fig. 2A). For the abyssal-cell, there is a portion of the flow that is deeper than our deepest moorings which is unsampled. As a result, the vertical integration cannot go from the sea-floor up to the zero crossing of the transport per unit depth profile in a parallel manner to what was done for the upper-cell. Instead, the abyssal-cell upper vertical integration limit is chosen to be the point where the cumulative transport from the surface downward reaches zero (mean depth of 3155 dbar; i.e., the black dot in Fig. 2A where shallow and deep limbs of the upper-cell have perfectly balanced to yield mean zero cumulative transport). The lower integration limit for the abyssal-cell is chosen as the point where the transport per unit depth profile changes from southward (i.e., the upper limb of the abyssal-cell) to northward (mean depth of 4295 dbar; blue dot in Fig. 2A). Temporally constant integration limits were thus used for the upper and abyssal transports. Tests with time-varying integration limits that vertically followed the instantaneous zero velocity crossings when both cells are detected (75% of the time) show standard deviations of 484 dbar and 327 dbar for the upper (red dot in

Fig. 2A) and lower (blue dot in Fig. 2A) interface boundaries, respectively. The resulting transport time series are not highly sensitive to modest changes (within these standard deviations) in the vertical integration limits (as evidenced by correlations of r = 0.99 for both cells with transports computed using time-varying vs. time-mean vertical integration limits).

The seasonal anomalies of the MOC volume transport time series (Fig. 3) are determined using the continuous daily 2013-2017 data, with each daily climatology smoothed with a second-order Butterworth low-pass filter using a 90-day cutoff period passed both forward and backward to avoid phase shifting. This filtering is applied to a three-repeating-year climatology, and only the central year is kept to eliminate edge effects/transients in the smoothed climatology. Error bars indicated in the upper left of each panel represent plus/minus one standard error. The standard error is calculated as the standard deviation of the difference between the 90-day low-pass filtered daily data and the corresponding daily climatology, divided by the square-root of the number of years of data available. We assume with four years of data we have four independent degrees of freedom, which is a fairly conservative estimate.

Transports Accuracy Estimates

Because of the sloping topography, SAMBA allows transport calculations from the surface down to 4700 dbar, with some small regions that are not sampled on the upper slopes and continental shelves, in the bottom triangles and below the deepest common depth of the interior moorings. The observing system that collected the measurements we describe here is still in the water, with two new instruments in the interior added to the array in 2019, and future augmentations are planned on both boundaries. Bottom triangles and limited shelf observations are a common problem of all of the trans-basin MOC arrays, however the errors associated with these unobserved regions can be quantified (see below), and with these additional planned moorings these shortcomings will be improved for this array in the future.

The transport accuracy estimates have been derived following the methods described within the appendices of *(21)* and *(39)*. Following these techniques, we have separated the sources of error in the transport as being random or biases (Table S2). In this study, all the errors are calculated separately for the upper and abyssal transports. Those sources of errors that are independent of one another are combined via a standard square root of the sum of squares method to yield the overall accuracy estimate. A detailed explanation of the sources of error can be found in *(21)*; here only a brief discussion is presented, focusing primarily on the specifics of this application.

As described by *(21)*, there are several accuracy issues that can apply to the τ measurements of the PIES. To convert the different τ based accuracies into equivalent volume transport accuracies, a linear relationship between the vertical integral of the dynamic height anomaly (i.e., the baroclinic streamfunction, also sometimes called the Fofonoff Potential, χ) and τ was used; separate linear relationships were determined for the western and eastern portions of SAMBA using hydrography from those regions. The vertical integration domain for the Fofonoff potential was selected to be consistent with the vertical boundaries used for the transport integrals themselves, that is, between the surface and 1315 dbar for the upper-cell and between 3155 and 4295 dbar for the abyssal-cell. The resulting χ based accuracy estimates were then converted into transport errors assuming a constant density of 1030 kg m^{-3} and the appropriate local Coriolis parameter.

The random accuracy of the geostrophic velocity (or transport) relative to an assumed level of no motion is a function of four terms: (1) the accuracy of measured τ from the instrument (0.5 ms; *(40)*); (2) the scatter in the calibration relationship that converted τ at the depth of the PIES into the equivalent τ at 1000 dbar; (3) the accuracy of the GEM lookup tables; and, (4) the scatter introduced by projecting the τ at 1,000 dbar (and their derived dynamic height profiles) downward using the GEM lookup tables to the deepest vertical integration boundary (1315 dbar for the upper-cell and 4295 dbar for the abyssal-cell). The accuracy of the reference velocity is dependent on the accuracy of the pressure gauges (0.01 dbar; *(40)*) which is added as a random source in the final absolute geostrophic velocities (transports). For the upper-cell, in addition to these terms, an additional Ekman transport accuracy must be added. The Ekman accuracy was estimated by calculating the root-mean-squared difference between Ekman transports determined from the CCMP wind product and Ekman transports determined from an independent wind product (see *(21)* for more details). Estimates of the accuracy associated with the unmeasured transport by flows on the shallow continental shelves and upper slopes were made via comparisons to independent data sets and numerical models. All these errors were estimated following the methods shown in *(21)* and *(39)*. When all of the sources of random errors are combined, we find total random errors of 6.4 Sv for the daily upper-cell transport estimates and 6.3 Sv for the daily abyssal-cell transport estimates (Table S2).

In addition to random errors affecting the time variability of the transport, some errors can affect the time-mean transport. Following the methods presented in *(21)*, two potential sources of error were considered for both the upper and abyssal cell transports that apply to the time-mean but not to the time variability: (1) the mean offset/calibration of the PIES measured τ into the equivalent τ at 1000 dbar; and, (2) the accuracy of the applied time-mean reference velocity. The Ekman transports and the unobserved meridional flows on the upper slopes and continental shelves can also have potential time-mean biases, which were estimated following the methods of *(21)* and included as bias sources for the upper-cell. Finally, the time-mean bias associated with unobserved flows in the deep bottom triangles, was estimated following the method described in the preceding section “Data and Method”, and included as bias source for the abyssal-cell.

The sources of bias are assumed to be as independent of one another, so they can also be combined via a square root of the sum of squares method, yielding 5.0 and 2.7 Sv as the potential bias errors in the time-mean upper and abyssal cell transports, respectively (Table S2).

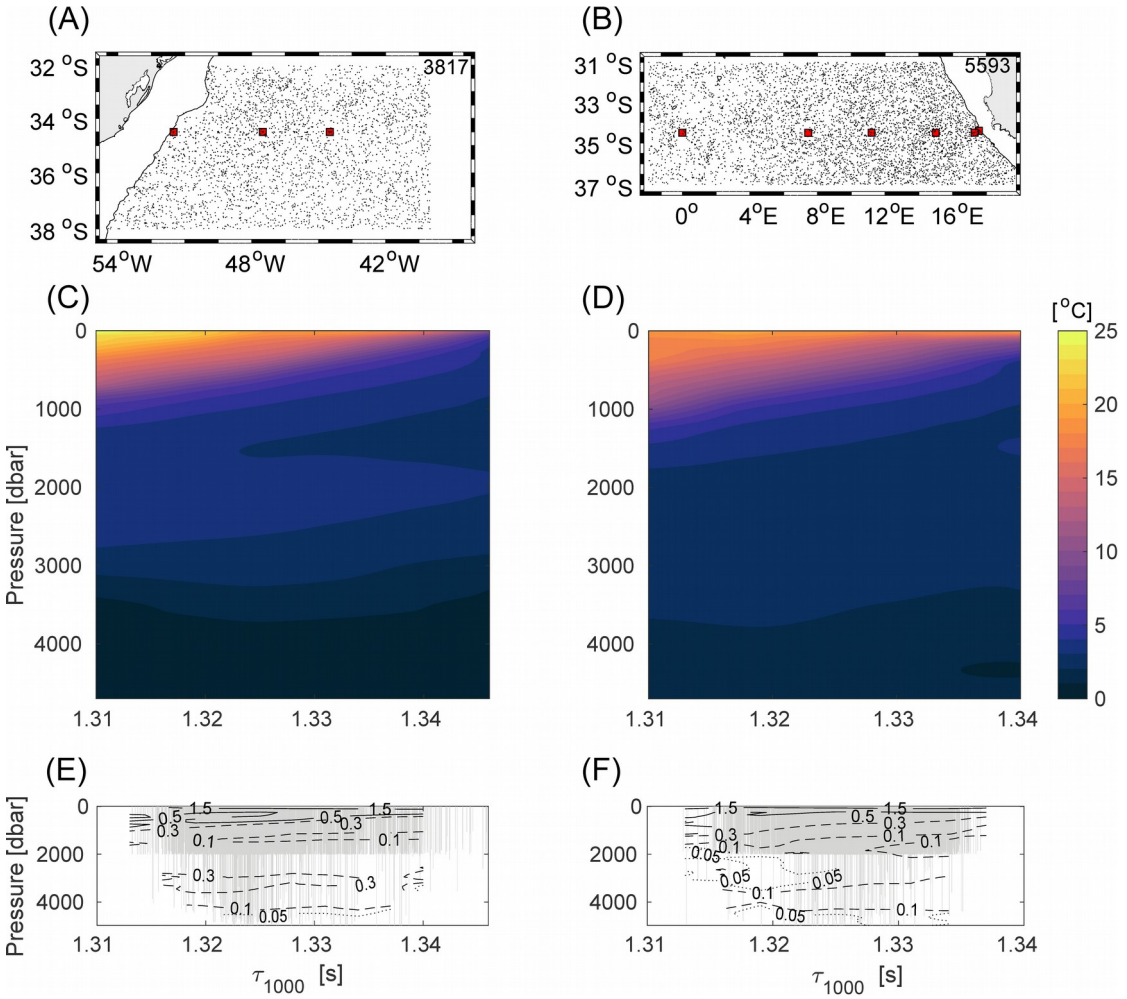

Fig. S1. GEM fields of temperature determined for the western boundary (left column), and the eastern boundary (right column). (A, B) Positions of the CTD and Argo casts collected around SAMBA transect and used to create the GEM fields. The PIES locations are identified by the red squares. Numbers indicated in the upper right represent the numbers of profiles used to create the GEM fields. (C, D) GEM fields of temperature as a function of pressure and τ. (E, F) The root-mean-square differences between the original hydrographic measurements and the GEM lookup table values. The solid, dashed, and dotted contours represent progressively smaller contour intervals, with values labeled in °C. The gray vertical lines show the locations of the hydrographic (CTD and Argo) measurements.

Site name	Mooring type	Latitude	Longitude	Water depth
A	PIES	34°30.00′S	51°30.00′W	1360 m
C	PIES	34°30.00′S	47°30.00′W	4540 m
D	PIES	34°30.00′S	44°30.00′W	4757 m
S	CPIES	34°30.06′S	0°0.02′E	4608 m
U	CPIES	34°30.42′S	7°27.03′E	5185 m
V	CPIES	34°30.00′S	11°12.19′E	4969 m
W	PIES	34°30.25′S	15°0.16′E	4482 m
Y	CPIES	34°29.81′S	17°18.04′E	2129 m
Z	CPIES	34°24.35′S	17°33.46′E	1266 m

Table S1. Nominal locations and depths of the PIES and CPIES moorings which were all in place continuously during September 2013-July 2017, and which are discussed in this paper. Note: the first instrument at Site W was a CPIES, but it was replaced with a PIES in September 2015. Additional moorings have been deployed in the array, however only the sites that have been in place for the entire time period that is discussed in this paper are listed here. For simplicity in the main text, we refer to the CPIES as PIES.

	Accuracy Estimate	
Random Sources	**Upper**	**Abyssal**
Measured τ accuracy	1.5 Sv	0.6 Sv
Scatter in τ PIES versus τ 1000	0.5 Sv	2.4 Sv
GEM look-up table accuracy	4.2 Sv	2.9 Sv
Baroclinic shear	1.2 Sv	4.6 Sv
Measured pressure accuracy	2.2 Sv	1.9 Sv
Ekman accuracy	1.4 Sv	*n.a.*
West shelf missed variability	2.5 Sv	*n.a.*
East shelf missed variability	2.5 Sv	*n.a.*
Total random	**6.4 Sv**	**6.3 Sv**
Bias Sources	**Upper**	**Abyssal**
Calibration of τ PIES with concurrent CTDs	4.8 Sv	2.0 Sv
Accuracy of reference velocity time-mean	1.4 Sv	0.9 Sv
Ekman time-mean accuracy	0.02 Sv	*n.a.*
Combined shelf missed time-mean	0.2 Sv	*n.a.*
Bottom triangles time-mean accuracy	*n.a.*	1.5 Sv
Total bias	**5.0 Sv**	**2.7 Sv**

Table S2. Estimates of the error contributions to the upper and abyssal transport accuracies.

REFERENCES AND NOTES

1. IPCC, *Climate Change 2013: The Physical Science Basis*, T. F. Stocker, D. Qin, G.-K. Plattner, M. B. Tignor, S. K. Allen, J. Boschung, A. Nauels, Y. Xia, V. Bex, P. M. Midgley, Eds. (Cambridge Univ. Press, 2013).

2. S. Rahmstorf, G. Feulner, M. E. Mann, A. Robinson, S. Rutherford, E. J. Schaffernicht, Exceptional twentieth-century slowdown in Atlantic Ocean overturning circulation. *Nat. Clim. Change* **5**, 475–480 (2015).

3. M. Rhein, Taking a close look at ocean circulation. *Science* **363**, 456–457 (2019).

4. A. Biastoch, C. W. Böning, J. R. E. Lutjeharms, Agulhas leakage dynamics affects decadal variability in Atlantic overturning circulation. *Nature* **456**, 489–492 (2008).

5. W. Weijer, W. Cheng, S. S. Drijfhout, A. V. Federov, A. Hu, L. C. Jackson, W. Liu, E. L. McDonagh, J. V. Mecking, J. Zhang, Stability of the atlantic meridional overturning circulation: A review and synthesis. *J. Geophys. Res.* **124**, 5336–5375 (2019).

6. R. Lumpkin, K. Speer, Global ocean meridional overturning. *J. Phys. Oceanogr.* **37**, 2550–2562 (2007).

7. L. D. Talley, Closure of the global overturning circulation through the Indian, Pacific, and Southern Oceans: Schematics and transports. *Oceanography* **26**, 80–97 (2013).

8. D. Valla, A. R. Piola, C. S. Meinen, E. Campos, Strong mixing and recirculation in the northwestern Argentine Basin. *J. Geophys. Res.* **123**, 4624–4648 (2018).

9. P. Cessi, The global overturning circulation. *Ann. Rev. Mar. Sci.* **11**, 249–270 (2019).

10. A. Ganachaud, C. Wunsch, Improved estimates of global ocean circulation, heat transport and mixing from hydrographic data. *Nature* **408,** 453–457 (2000).

11. S. L. Garzoli, M. O. Baringer, Meridional heat transport determined with expandable bathythermographs—Part II: South Atlantic transport. *Deep Sea Res. Part I* **54**, 1402–1420 (2007).

12. H. Lopez, S. Dong, S. K. Lee, G. Goni, Decadal modulations of interhemispheric global atmospheric circulations and monsoons by the South Atlantic meridional overturning circulation. *J. Climate* **29**, 1831–1851 (2016).

13. E. L. McDonagh, B. A. King, Oceanic fluxes in the South Atlantic. *J. Phys. Oceanogr.* **35**, 109–122 (2005).

14. H. L. Bryden, B. A. King, G. D. McCarthy, South Atlantic overturning circulation at 24°S. *J. Mar. Res.* **69**, 39–56 (2011).

15. A. Hernández-Guerra, L. D. Talley, J. L. Pelegrí, P. Vélez-Belchí, M. O. Baringer, A. M. Macdonald, E. L. McDonagh, The upper, deep, abyssal and overturning circulation in the Atlantic Ocean at 30°S in 2003 and 2011. *Prog. Oceanogr.* **176**, 102136 (2019).

16. S. Dong, S. L. Garzoli, M. O. Baringer, C. S. Meinen, G. J. Goni, Interannual variations in the Atlantic meridional overturning circulation and its relationship with the net northward heat transport in the South Atlantic. *Geophys. Res. Lett.* **36**, L20606 (2009).

17. S. L. Garzoli, M. O. Baringer, S. Dong, R. C. Perez, Q. Yao, South Atlantic meridional fluxes. *Deep-Sea Res. I Oceanogr. Res. Pap.* **71**, 21–32 (2013).

18. S. Dong, G. J. Goni, F. Bringas, Temporal variability of the South Atlantic meridional overturning circulation between 20°S and 35°S. *Geophys. Res. Lett.* **42**, 7655–7662 (2015).

19. S. Majumder, C. Schmid, G. Halliwell, An observations and model-based analysis of meridional transports in the South Atlantic. *J. Geophys. Res.* **121**, 5622–5638 (2016).

20. T. Kanzow, S. A. Cunningham, W. E. Johns, J. J.-M. Hirschi, J. Marotzke, M. O. Baringer, C. S. Meinen, M. P. Chidichimo, C. Atkinson, L. M. Beal, H. L. Bryden, J. Collins, Seasonal variability of the Atlantic meridional overturning circulation at 26.5°N. *J. Climate* **23**, 5678–5698 (2010).

21. C. S. Meinen, S. Speich, R. C. Perez, S. Dong, A. R. Piola, S. L. Garzoli, M. O. Baringer, S. Gladyshev, E. J. D. Campos, Temporal variability of the meridional overturning circulation at

34.5°S: Results from two pilot boundary arrays in the South Atlantic. *J. Geophys. Res.* **118**, 6461–6478 (2013).

22. C. S. Meinen, S. Speich, A. R. Piola, I. J. Ansorge, E. J. D. Campos, M. Kersalé, T. Terre, M. P. Chidichimo, T. Lamont, O. T. Sato, R. C. Perez, D. Valla, M. A. van den Berg, M. Le Hénaff, S. Dong, S. L. Garzoli, Meridional Overturning Circulation transport variability at 34.5°S during 2009-2017: Baroclinic and barotropic flows and the dueling influence of the boundaries. *Geophys. Res. Lett.* **45**, 4180–4188 (2018).

23. E. Frajka-Williams, M. Lankhorst, J. Koelling, U. Send, Coherent circulation changes in the Deep North Atlantic from 16°N and 26°N transport arrays. *J. Geophys. Res.* **123**, 3427–3443 (2018).

24. D. Desbruyères, E. L. McDonagh, B. A. King, V. Thierry, Global and full-depth ocean temperature trends during the early twenty-first century from argo and repeat hydrography. *J. Climate* **30**, 1985–1997 (2017).

25. N. Hogg, P. E. Biscaye, W. D. Gardner, W. J. Schmitz Jr., On the transport and modification of Antarctic Bottom Water in the vema channel. *J. Mar. Res.* **40**, 231–263 (1982).

26. W. Zenk, G. Siedler, B. Lenz, N. G. Hogg, Antarctic bottom water flow through the hunter channel. *J. Phys. Oceanogr.* **29**, 2785–2801 (1999).

27. M. Arhan, H. Mercier, Y. H. Park, On the deep water circulation of the eastern South Atlantic Ocean. *Deep-Sea Res. I Oceanogr. Res. Pap.* **50**, 889–916 (2003).

28. R. C. Perez, S. L. Garzoli, C. S. Meinen, R. P. Matano, Geostrophic velocity measurement techniques for the meridional overturning circulation and meridional heat transport in the South Atlantic. *J. Atmos. Oceanic Tech.* **28**, 1504–1521 (2011).

29. R. E. Thomson, W. J. Emery, *Data Analysis Methods in Physical Oceanography* (Elsevier Science, ed. 3, 2014), pp. 728.

30. R. O. R. Y. Thompson, Coherence significance levels. *J. Atmos. Sci.* **36**, 2020–2021 (1979).

31. S. A. Cunningham, T. Kanzow, D. Rayner, M. O. Baringer, W. E. Johns, J. Marotzke, H. R. Longworth, E. M. Grant, J. J.-M. Hirschi, L. M. Beal, C. S. Meinen, H. L. Bryden, Temporal variability of the Atlantic meridional overturning circulation at 26.5°N. *Science* **317**, 935–938 (2007).

32. T. Kanzow, S. A. Cunningham, D. Rayner, J. J.-M. Hirschi, W. E. Johns, M. O. Baringer, H. L. Bryden, L. M. Beal, C. S. Meinen, J. Marotzke, Observed flow compensation associated with the MOC at 26.5°N in the Atlantic. *Science* **317**, 938–941 (2007).

33. O. A. Saenko, On the strong seasonal currents in the deep ocean. *J. Climate* **21**, 5642–5656 (2008).

34. C. S. Meinen, D. R. Watts, Vertical structure and transport on a transect across the North Atlantic current near 42°N: Time series and mean. *J. Geophys. Res.* **105**, 21869–21891 (2000).

35. G. D. McCarthy, D. A. Smeed, W. E. Johns, E. Frajka-Williams, B. I. Moat, D. Rayner, M. O. Baringer, C. S. Meinen, J. Collins, H. L. Bryden, Measuring the Atlantic meridional overturning circulation at 26°N. *Prog. Oceanogr.* **130**, 91–111 (2015).

36. M. S. Lozier, F. Li, S. Bacon, F. Bahr, A. S. Bower, S. A. Cunningham, M. F. de Jong, L. de Steur, B. deYoung, J. Fischer, S. F. Gary, B. J. W. Greenan, N. P. Holliday, A. Houk, L. Houpert, M. E. Inall, W. E. Johns, H. L. Johnson, C. Johnson, J. Karstensen, G. Koman, I. A. Le Bras, X. Lin, N. Mackay, D. P. Marshall, H. Mercier, M. Oltmanns, R. S. Pickart, A. L. Ramsey, D. Rayner, F. Straneo, V. Thierry, D. J. Torres, R. G. Williams, C. Wilson, J. Yang, I. Yashayaev, J. Zhao, A sea change in our view of overturning in the subpolar North Atlantic. *Science* **363**, 516–521 (2019).

37. R. Atlas, R. N. Hoffman, J. Ardizzone, S. M. Leidner, J. C. Jusem, D. K. Smith, D. Gombos, A cross-calibrated, multiplatform ocean surface wind velocity product for meteorological and oceanographic applications. *Bull. Amer. Meteor. Soc.* **92**, 157–174 (2011).

38. H. E. Garcia, K. Weathers, C. R. Paver, I. Smolyar, T. P. Boyer, R. A. Locarnini, M. M. Zweng, A. V. Mishonov, O. K. Baranova, D. Seidov, J. R. Reagan, World Ocean Atlas 2018, Volume 3: *Dissolved Oxygen, Apparent Oxygen Utilization, and Oxygen Saturation*, A. Mishonov Technical Ed. (NOAA Atlas NESDIS 83, 2018).

39. M. Kersalé, R. C. Perez, S. Speich, C. S. Meinen, T. Lamont, M. Le Hénaff, M. A. van den Berg, S. Majumder, I. J. Ansorge, S. Dong, C. Schmid, T. Terre, S. L. Garzoli, Shallow and deep eastern boundary currents in the South Atlantic at 34.5°S: Mean structure and variability. *J. Geophys. Res.* **124**, 1634–1659 (2019).

40. K. A. Donohue, D. R. Watts, K. L. Tracey, A. D. Greene, M. Kennelly, Mapping circulation in the Kuroshio extension with an array of current and pressure recording inverted echo sounders. *J. Atmos. Ocean. Tech.* **27**, 507–527 (2010).